Physics in Medicine & Biology

PAPER • **OPEN ACCESS**

Laser-activated microparticles for multimodal imaging: ultrasound and photoacoustics

To cite this article: Mirjam Visscher *et al* 2019 *Phys. Med. Biol.* **64** 034001

IOP Publishing Phys. Med. Biol. 64 (2019) 034001 (14pp) https://doi.org/10.1088/1361-6560/aaf4a2

Physics in Medicine & Biology

IPEM Institute of Physics and Engineering in Medicine

OPEN ACCESS

PAPER

Laser-activated microparticles for multimodal imaging: ultrasound and photoacoustics

Mirjam Visscher[1,2], Guillaume Lajoinie[1], Emilie Blazejewski[3], Gert Veldhuis[3] and Michel Versluis[1,4]

[1] Physics of Fluids Group, Technical Medical (TechMed) Centre and MESA+ Institute for Nanotechnology, University of Twente, PO Box 217, 7500 AE Enschede, The Netherlands

[2] Department of Biomedical Engineering, Thorax Center, Erasmus University Medical Center, PO Box 2040, 3000 CA Rotterdam, The Netherlands

[3] Nanomi Monosphere Technology, Zutphenstraat 51, 7575 EJ Oldenzaal, The Netherlands

[4] Author to whom any correspondence should be addressed.

E-mail: m.versluis@utwente.nl

Keywords: photoacoustics, ultrasound, contrast agents, cavitation, polymeric microcapsules

Supplementary material for this article is available online

RECEIVED
8 June 2018

REVISED
30 October 2018

ACCEPTED FOR PUBLICATION
28 November 2018

PUBLISHED
29 January 2019

Abstract

The increasing personalization of medical treatment demands refined imaging and increased monitoring capabilities, as well as an improved efficacy through targeted drug delivery. Such a transition in health care can be facilitated by the use of multimodal contrast agents. In this paper, we present a novel type of multimodal contrast agents, that enhances contrast both in ultrasound and in photoacoustic imaging, while at the same time being capable of triggered drug delivery. Upon pulsed laser irradiation, polymeric microparticles—containing a dye and an oil core—can create a cavitation bubble that subsequently emits a strong acoustic wave. We investigated different formulations of these particles, by changing the oil content, dye concentration and probing conditions using a combination of pulsed laser excitation and an ultrasound chirp. We demonstrated that capsules with a core containing a low boiling point oil give the highest photoacoustic and acoustic response. The laser activation threshold for this system is high in the visible range, but within the near infrared medical limits. The same system also produces a stable bubble. US scattering by these stable bubbles results in medically relevant frequencies, making the particles of interest for biomedical and pre-clinical imaging. Finally, the system has potential to carry a functional drug-load, and a route to these applications is discussed.

1. Introduction

Medical care at present is facing challenges in the diagnosis and treatment of a number of diseases, such as cancer or genetic deficiencies. These challenges seem to fall beyond the limits of traditional pharmaceutical industry and call for new strategies. One such strategy is to deliver targeted and personalized care to account for the individual differences within the patient population. An implicit requirement to ensure success of such a strategy is the ability to provide early diagnosis and to precisely control the targeted therapeutic effects. For targeted drug delivery applications, this implies refined imaging and monitoring capability as well as an increased level of precision.

A modality that would meet these requirements is ultrasound (US). US is of particular interest as an affordable bedside technique, offering an unrivaled combination of resolution, a good imaging depth, and an outstanding safety record. Traditional US imaging relies on the variation of elastic and mechanical properties within tissue. However, this method has the disadvantage of providing relatively weak contrast and low specificity. The first issue can be addressed by making use of US contrast agents that typically consist of phospholipid-coated microbubbles (Calliada *et al* 1998, Overvelde *et al* 2010). These bubbles undergo volumetric oscillations upon exposure to a US field, leading to a strong acoustic scatter that greatly improves contrast (De Jong 1993). Additionally, these oscillations demonstrate great potential for therapeutic applications, for example, by temporarily porating cell membranes to aid the delivery of a drug (Husseini and Pitt 2009). Several studies have

demonstrated an increased cell membrane permeability in the presence of cavitating microbubbles, a process called sonoporation (Szabo 2004, Deckers *et al* 2008, Frenkel 2008, Chen *et al* 2011). Other therapeutic applications such as blood-brain-barrier opening are currently under clinical investigation (Hynynen *et al* 2006, Choi *et al* 2011, Wei *et al* 2013).

Another potential candidate for meeting the newly set standards in medical care is photoacoustics (PA). The contrast generation in PA imaging is based on the optical absorption of tissue components. Light is absorbed by chromophores in the tissue that rapidly heats up, leading to thermal expansion and subsequent relaxation of the absorbing material (Bell 1880, Mallidi *et al* 2011). This transient dilatation generates a pressure wave, which can be detected in the far field and converted into an image. The large variation in optical properties amongst tissues makes PA imaging intrinsically more specific than US imaging while maintaining the spatial resolution of US imaging. Such improvement, however, is made at the cost of a much reduced penetration depth, typically limited to 1 cm (Mallidi *et al* 2011). Here as well, contrast agents have been developed to address the penetration issue, and these include dyes (Kim *et al* 2007, Bhattacharyya *et al* 2008, Stantz *et al* 2010), nanoparticles (Li *et al* 2006, Mallidi *et al* 2009, Bayer *et al* 2011), microbubbles with dyed coatings (Jeon *et al* 2014, Lajoinie *et al* 2017a, 2017b), polymeric microcapsules (Lajoinie *et al* 2014, Yue *et al* 2017) and microdroplets (Wilson *et al* 2010). These agents improve contrast by either absorbing light at a more favorable wavelength, within the tissue optical window, or by presenting an order of magnitude stronger absorption than native chromophores (Luke *et al* 2012). The use of metallic (gold, silver) nanoparticles has been predominantly investigated due to the possibility of tuning the absorption wavelength and the large absorption cross-section provided by their plasmon resonance (Choi *et al* 2011, Luke *et al* 2012). Nanotoxity of metallic agents, however, remains a serious concern (Luke *et al* 2012, Khanna *et al* 2015).

The image acquisition principle in both US and PA imaging is identical. Both modalities therefore require very similar equipment and are, in practice, easy to combine in order to benefit from their complementary characteristics. Multimodal imaging with US and PA has been used for intra-vascular detection of vulnerable plaques (Wu *et al* 2017) and for US-guided PA imaging of tumors (Mallidi *et al* 2015a). Microdroplets (Wilson *et al* 2012), coated microparticles (Shih *et al* 2013, Lajoinie *et al* 2017a), and gold nanoparticles (Lu *et al* 2010, Wilson *et al* 2012, Mallidi *et al* 2015b) have been proposed as agents that are both, stronger PA emitters and responsive to US. Additionally, some of these agents have been investigated for their capability to vaporize upon optical or acoustical triggering, leading to the formation of bubbles (Wilson *et al* 2012) capable of generating contrast for US imaging (De Jong 1993).

Here, we investigate the multimodal capabilities of micron-sized polymeric capsules doped with an absorbing dye located in the capsule shell. Such capsules can be triggered by a laser, leading to vaporization and formation of a bubble (Lajoinie *et al* 2014, 2017a). In our earlier work (Lajoinie *et al* 2014, 2017a), we have established the basic physical requirements on these cavitation systems and in particular the need for the melting point of the polymer shell to be slightly above the boiling temperature of the liquid in order to induce the vaporization. In this paper, we extend the original high boiling point formulation, first, to a low boiling point formulation that vaporizes preferentially its liquid core rather than the surrounding water and, second, to a different geometrical configuration where the oil is only partially encapsulated, resulting in a total of three particle types. The first formulation consists of PMMA polymer and a high boiling point oil core (hexadecane). The second formulation consists of a low glass transition temperature polymer shell (Resomer, $T_g \sim 50$ °C), filled with a low boiling point oil (perfluoropentane). This last formulation was also produced in a Janus configuration, referred to as 'cups', to further reduce the activation threshold at the price, however, of a reduced overall stability. We experimentally investigate both the PA and US contrast enhancement capabilities of the particles by subjecting them first to a laser light pulse before probing the resulting bubbles with an ultrasound chirp within a few milliseconds.

2. Materials and methods

2.1. Materials

Gold nanospheres (20 nm, 5.9×10^{11}–7.2×10^{11} particles ml^{-1}), Sodium cholate hydrated, Polyvinyl alcohol (PVA), Poly(lactide-co-glycolide) Resomer RG502 (MW 7-17 and MW 28-34), Poly(methyl methacrylate) (MW 120 000), hexadecane, Sudan Red, Nile Red and dichloromethane (ACS reagent) were purchased from Sigma-Aldrich (St. Louis, MO, USA). PDLG 5002, PDLG 5004 and PDL 02 were provided by Purac. Perfluoropentane (PFP), Perfluoropentane (PFP) and 1-Bromoperfluorooctane (PFOB) were purchased from Fluorochem (UK). Tween 20 was purchased from VWR (The Netherlands).

2.2. Capsules fabrication

PMMA microcapsules were prepared by a emulsion solvent evaporation technique using microsieve emulsification (Loxley and Vincent 1998). Prior to emulsification, the oil ($T_b = 286$ °C), the polymer

($T_g = 102$ °C) and the dye were dissolved in dichloromethane. The oil concentration was 2.16% w/w in the solution and the dye concentration was 4.85% w/w as compared to the polymer.

Resomer microcapsules containing perfluorocarbon were fabricated in a similar way as the PMMA capsules. Resomer ($T_g = 50$ °C) was dissolved into dichloromethane along with perfluorocarbon oil ($T_b = 29$ °C) and the dye and subsequently placed in a 20 °C bath to ensure the full miscibility of the oil in dichloromethane. The oil concentration was 2.42% w/w in the solution and the dye concentration was 4.89% w/w as compared to the polymer.

The solutions were filtered through a 0.45 μm PTFE filter and emulsified through a micro sieve membrane (Nanomi B.V., The Netherlands) with uniform pores along the surface. The emulsions were then dispersed into an aqueous solution containing an emulsifier. This was left to stir at room temperature for at least 3 h to evaporate the dichloromethane, the process is depicted in figure 1(a). The hardened microcapsules were subsequently concentrated and washed repeatedly using vacuum filtration and using 0.05% w/w Tween 20 solution. The washed suspension was stored at 4 °C until further use. Details on the capsules production process are given in SI-1 (stacks.iop.org/PMB/64/034001/mmedia).

2.3. Sample preparation

First, a reference concentration of gold nanospheres was chosen, with an absorption coefficient of $\sim$0.07 cm^{-1}. In order to get a fair comparison between the various agents investigated, the concentration of PMMA-hexadecane capsules suspension was set to match the extinction coefficient of our reference sample, which required a 40× dilution of the native sample. The concentration of the Resomer-PFP capsules suspension was prepared to roughly match the concentration of the PMMA-hexadecane capsules suspension, corresponding to a 20× dilution of the native sample. The same dilution was applied to the Resomer-PFP cups.

The contrast agents were investigated in a set of experimental conditions: (1) at room temperature and (2) at body temperature, where the sample was heated to 37 °C prior to the experiment (heating bath, Medingen WB6).

2.4. Experimental setup

We tested the contrast-enhancing capabilities of the capsules *in vitro*. A schematic of the experimental setup is displayed in figure 2(a). The sample was illuminated using a laser beam (Quantel Evergreen, 150 mJ, 532 nm, 15 Hz, 8 ns) to activate the capsules. The fluence of the laser beam was regulated by a computer-controlled attenuator. The laser spot size was confined using a 1 mm diameter diaphragm, ensuring uniform laser spot size and homogeneous energy density. The beam was directed through the tank before reaching a beam-dump. The laser fluence was measured using an energy meter (Coherent FieldMaxII-P).

The samples were inserted into a water-tight sample holder, placed in a temperature-controlled water bath. The lateral sides of the sample holder are made of glass, and the back of the sample holder consists of PDMS to damp the acoustic wave passing through the sample during the acoustic characterization and to minimizes the acoustic reflections from the sample. The PDMS also allowed for easy insertion of tubes in order to circulate the sample in the sample holder continuously, ensuring the reproducibility of the measurement. The front plane is made from a highly acoustically transparent Opticell® membrane. The sample holder was set at a 40° angle to the transducer as to avoid interferences from acoustic reflections.

The signals were recorded by an oscilloscope (Tektronix DPO4034 Digital Phosphor) and saved to a computer. The experiment was computer-controlled and automatized using Matlab®. The timing of the experiment was controlled using a pulse-delay generator (BNC model 575) also controlled using Matlab®.

2.5. Photoacoustic measurements

The suspension was circulated in a sample holder where it was constantly refreshed, ensuring the presence of new capsules in the laser beam for each exposure. The suspension was irradiated with a laser fluence ranging from 3.3 mJ cm^{-2} to 322 mJ cm^{-2}. At each energy setting, the laser was fired 10 times. The resulting PA response was recorded with a focused broadband 1 MHz center frequency US transducer (C302 Panametrics—90% *BW*) after which the signal was amplified 25× (RF preamplifier, Stanford Research Systems inc. model SR445A). The processing of the data was performed in Matlab®. The final curves, displayed in this paper, are obtained after averaging the peak-to-peak pressure amplitude over ten recordings made for each energy setting.

2.6. Ultrasound characterization

After activation of the capsules by the pulsed laser, the capsules were acoustically characterized. The 1 MHz transducer was used to transmit a chirp with a ramp-up frequency from 0.3 to 2.3 MHz for a total pulse length of 200 μs and the echo was subsequently recorded. The frequency versus time content of the ultrasound burst used to probe the bubbles produced post laser activation is depicted in figure 2(b). The frequency content of the chirp was linearly swept with a fixed amplitude (Michaels *et al* 2013):

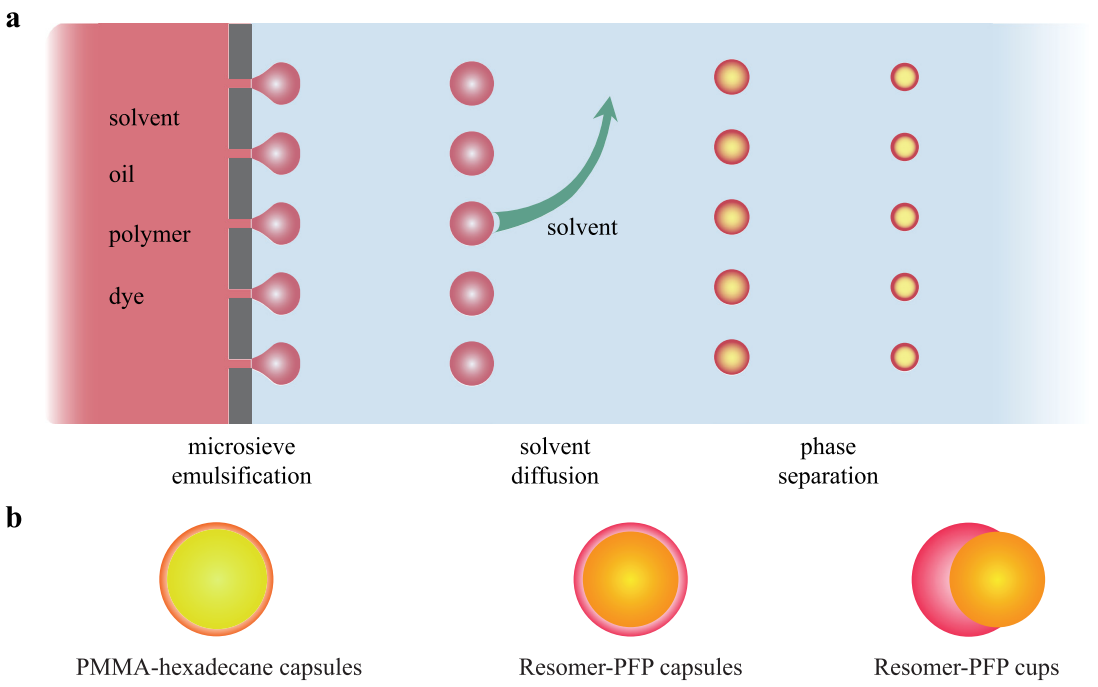

Figure 1. Schematic production process. (a) Microcapsule fabrication process in time, on the left the emulsification process with the solvent, the oil, the polymer and the dye. The solution is pushed through the microsieve into an aqueous solution, which is stirred while the solvent evaporates. The polymer and oil are immiscible resulting in a phase separation between oil and polymer, while the dye precipitates with the polymer. (b) Resulting microcapsule configurations.

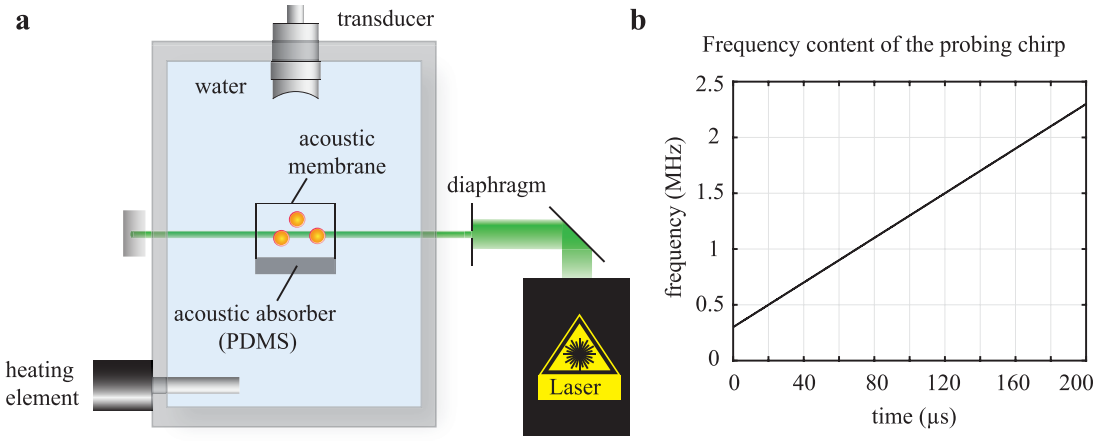

Figure 2. Schematic of the experimental setup. (a) A water tank containing the sample through which the laser is fired. The PA response of the capsules in the sample is then recorded by a focused 1 MHz US transducer. (b) Frequency versus time plot used for the excitation chirp for acoustic characterization.

$$s = w \sin\left(2\pi t\left(f_0 + \frac{\pi BWt}{T}\right)\right), \quad (1)$$

where f_0 is the starting frequency, BW is the bandwidth of the chirp, T is the duration of the chirp and w is the amplitude.

To avoid overlap with reflections traveling back to the transducer, the chirp was cut into four segments, resulting in a set of four chirps of 0.3–0.8, 0.8–1.3, 1.3–1.8 and 1.8–2.3 MHz. The routing of the signals (recording of the cavitation signal, emission of the chirp and recording of the chirp echo) was ensured by a custom-built high-voltage/low-noise electronic switch. In order to monitor the evolution of the bubbles over time the set of chirps was sent 8 times for each recording.

The chirp was generated using an arbitrary waveform generator (Tabor Electronic 1000 MS s^{-1}). The echo signals were amplified 25× (RF preamplifier, Stanford Research Systems inc., model SR445A).

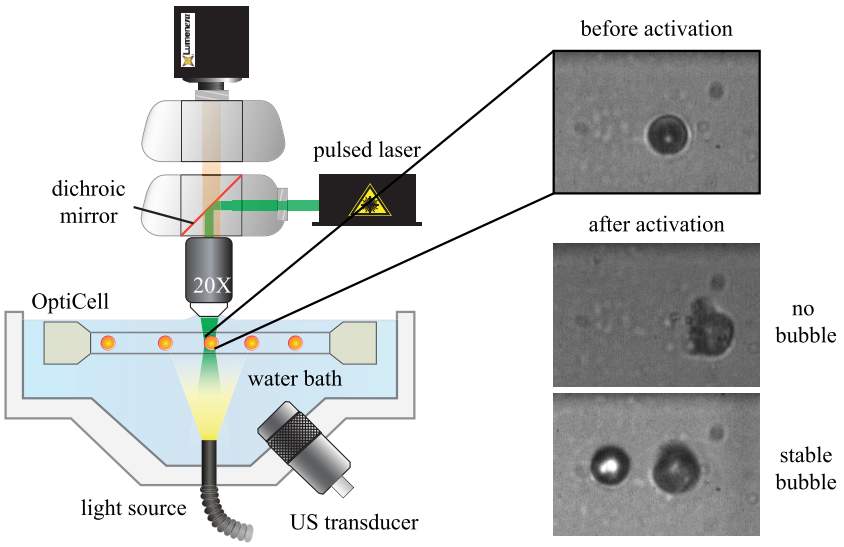

Figure 3. Schematic of the experimental setup for monitoring stable bubble formation of single microcapsules. Images from the CCD camera showing the appearance of the microcapsules, before activation and after activation, when there is no stable bubble remaining and, when a stable bubble is produced.

The pressures emitted and received during the acoustic characterization were estimated from the calibration of the transducer. The transducer was first calibrated in transmit, using a needle hydrophone (0.2 mm, Precision Acoustics, UK); and then in reception using the reflection from a flat metal plate (Chen *et al* 1994, Sijl *et al* 2008).

Acoustic scatter maps were computed by taking the envelope of the received US scatter signal at a specific fluence and taking the average over of all eight chirps sent. This was repeated for every fluence and the result was stacked to produce the scatter map. The standard deviation maps are provided in SI-7.

2.7. Single capsules cavitation

A second setup was built to record the response of single microcapsules using an optical microscope. The schematics of this setup is shown in figure 3. A suspension of microcapsules was injected into an OptiCell® and a single microcapsule was located using a water-immersion objective (LUMPLFL 20×, Olympus). The capsules were excited with an 8 ns laser pulse at a wavelength of 532 nm (Quantel Evergreen 150 mJ). The PA response was monitored with a focused broadband 1MHz US transducer (C302 Panametrics). The response of the microcapsules was recorded using a CCD camera (LM165m, Lumenera, CA) at low frame rate. These recording were too slow to visualize the cavitation dynamics but allow for sizing of the bubbles remaining after laser activation. From the images it was determined whether a cavitation event had taken place (through capsule destruction) and if a stable bubble was produced. We then calculated the probability of this cavitation event. The probability was calculated as the ratio between capsules that experienced cavitation and the total number of capsules tested.

The scattering properties of a free gas bubble in the presence an acoustic wave is well-known and well-documented (Leighton 1994). De Jong (1993) have shown that the scattering cross-section of an air bubble was 100 million times larger than that of a rigid sphere of the same size. These enhanced acoustic properties are primarily due to the compressibility of the gas (De Jong 1993), which allows for the system to resonate under US irradiation near its eigenfrequency (Szabo 2004). This resonance frequency for a free bubble can be derived from the Rayleigh–Plesset equation and is dependent on the inertia of the surrounding liquid and inversely proportional to the size of the bubble (Doinikov *et al* 2009, Overvelde *et al* 2010):

$$f_r = \frac{1}{2\pi R_0}\sqrt{\frac{1}{\rho}\left(3\kappa P_0 + (3\kappa - 1)\frac{2\sigma}{R_0}\right)}, \tag{2}$$

with f_r the resonance frequency, R_0 the equilibrium radius of the bubble, P_0 the ambient pressure, κ the polytropic exponent of the gas, ρ the density of the surrounding liquid and σ is the interfacial tension of the bubble. An expression neglecting the surface tension effects was already derived 80 years ago by Minnaert (Leighton 1994, Szabo 2004, Overvelde *et al* 2010):

$$f_r R_0 \approx 3.28\ \text{MHz} \cdot \mu\text{m}. \tag{3}$$

The response of the remaining bubbles to an US pulse can be calculated using the Keller–Miksis equation (Keller and Miksis 1980, Prosperetti and Lezzi 1986, Hilgenfeldt *et al* 1998), as a compressible alternative to the Rayleigh–Plesset equation:

$$\frac{1}{\rho}(R\ddot{R}+\frac{3}{2}\dot{R}^2) = P_g(R,t)-P(t)-P_0-\frac{R}{c_s}\frac{d}{dt}P_g(R,t)-\frac{4\mu\dot{R}}{R}-\frac{2\sigma}{R}, \quad (4)$$

where ρ the density of the surrounding medium, R is the radius of the bubble, P_g is the pressure of the gas, $P(t)$ is the US driving pressure, P_0 the ambient pressure, c_s the speed of sound in the medium, μ the viscosity of the surrounding liquid and σ is the surface tension of that liquid. The corresponding scattered pressure in the incompressible liquid is obtained from the conservation of mass and momentum (Versluis *et al* 2000):

$$P_{scat}(r,t) = \rho\frac{R}{r}\left(R\ddot{R}+2\dot{R}^2\right). \quad (5)$$

Under the first-order assumption that the capsules concentration is low, we neglect bubble–bubble interactions. A justification for this simplification is provided in SI-4. The response of the ensemble can then be calculated by summing the individual bubble responses, with an initial size distribution according to the measured distribution (De Jong 1993):

$$P_r(F) = \int_{R_0=0}^{R_0=10} P_e(R_0)\,p(R_o|F)dR_0, \quad (6)$$

where $P_r(F)$ is the pressure received by the transducer, $P_e(R_0)$ is the pressure emitted by a bubble of radius R_0, $p(R_0|F)$ is the probability of a bubble having a radius R_0 for a given fluence F (i.e. $p(R_0)$ knowing F). Using the results of single capsule experiments and equations (4)–(6), a pressure response map can be computed for PFP-Resomer capsules for frequencies in the range of 0.3–2.3 MHz and fluences ranging from 3 to 322 mJ cm^{-2}.

The scattering of the acoustic wave by the transiently stable bubbles created by the cavitation events was simulated by first fitting a Gaussian probability function to the size distribution obtained during single capsules experiments. The Gaussian distribution was then used to integrate the Rayleigh–Plesset equation using the Matlab® `ODE45`-solver for the different fluences used. This procedure resulted in a prediction of the frequency response of the bubble population generated by the laser pulse.

3. Results

Most combinations of polymer and oil have shown to result in cup shaped capsules, see SI-1 for details. Resomer in combination with PFP and PMMA in combination with hexadecane, however, have the right interfacial energies to result in core-shell shaped capsules. Final size of the capsules are $6 \pm 1\,\mu$m and $5 \pm 1\,\mu$m for PMMA-Hexadecane and Resomer-PFP, respectively. Size distributions of the capsules are shown in SI-1. Here, we also test Resomer-PFP cups that produced with a same polymer and oil than the capsules, except for a higher molecular weight, in order to investigate the effect of morphology on the PA and US behavior of the capsules, see figure 1(b) for a summary of the three particles tested here.

3.1. Photoacoustic response

Figures 4(a)–(d) depict the temporal PA response of AuNPs, PMMA-hexadecane capsules, Resomer-PFP capsules and Resomer-PFP cups for increasing fluence, respectively. The PA response for the AuNP has an amplitude of only 0.15 kPa at the maximum fluence. In contrast, the microcapsules generated large PA signatures with a formulation-dependent amplitude and shape.

At low fluence PMMA-hexadecane and Resomer-PFP particles display a similar bi-polar response pulse. At higher laser fluences, however, as cavitation starts to occur, the response shifts towards a tri-polar pulse. This third peak originates from the large positive acceleration during final bubble collapse. This last peak is then followed by secondary oscillations corresponding to the free oscillation, or ringing, of bubbles that remained after laser activation.

In figures 4(e)–(h) the ratio between the first and third peak is shown as a function of the fluence. The large amplitude ratio and large deviation at low fluence is due to a very low signal to noise ratio in the recorded waveforms. In these plots, the activation threshold of the microcapsules corresponds to a clear jump in the peak pressures ratio. Resomer-PFP capsules and cups generate secondary oscillations above ~75 mJ cm^{-2} and ~60 mJ cm^{-2}, respectively. This threshold reduction is consistent with the incomplete encapsulation of the oil in the cups, which therefore do not have to break open their shell (Lajoinie *et al* 2014).

In the absence of a volatile oil, PMMA-hexadecane capsules mainly generate transient water vapor bubbles that collapse and disappear. Nonetheless, above ~150 mJ cm^{-2}, gas intake by the cavitation bubble becomes

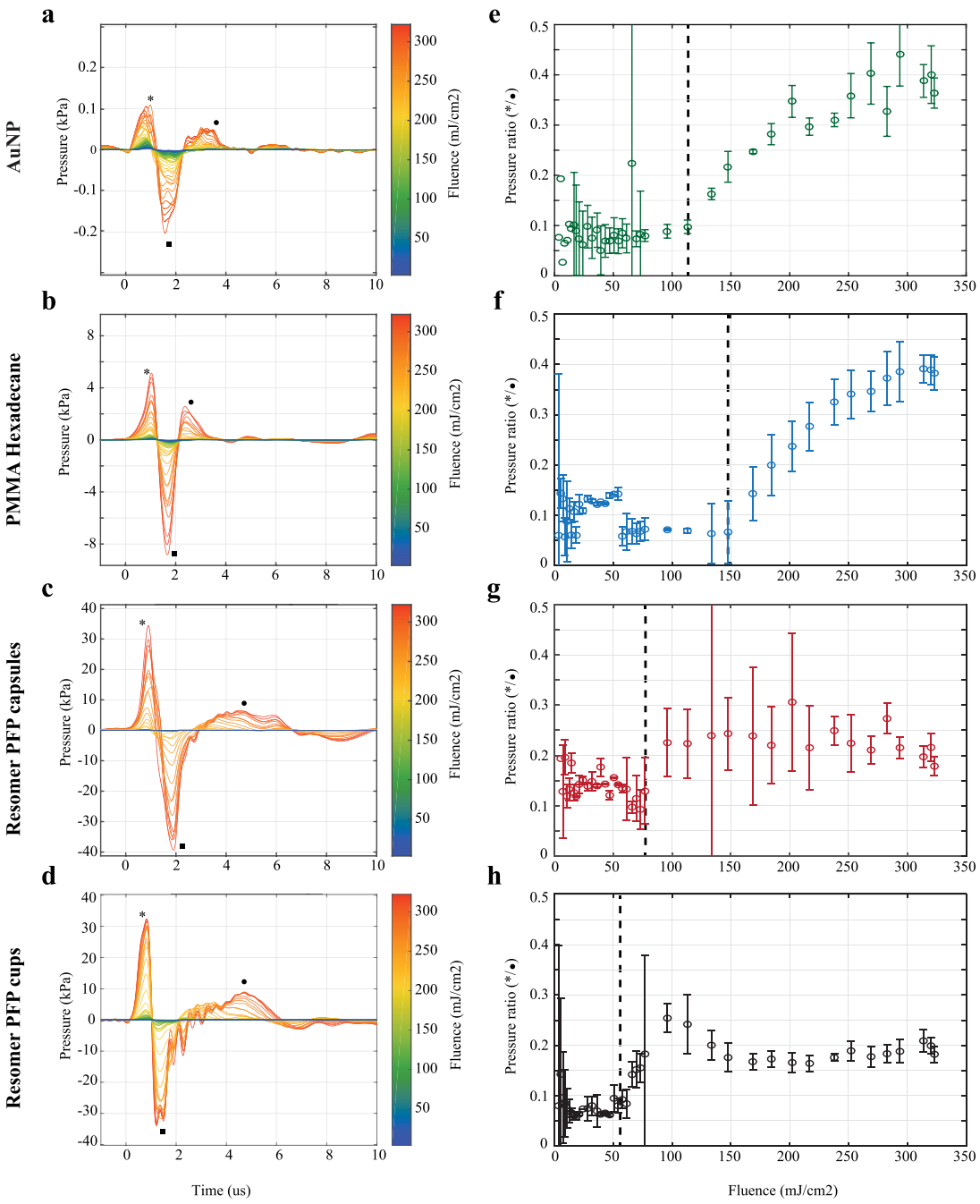

Figure 4. Photoacoustic response of (a) AuNP (b) PMMA-hexadecane capsules, (c) Resomer-PFP capsules, and (d) Resomer-PFP cups with marked peaks; ∗ peak 1, ■ peak 2 and • peak 3. Pressure ratio between first and third peak. (e) Gold nanoparticles. (f) PMMA-hexadecane capsules, (g) Resomer-PFP capsules, and (h) Resomer-PFP cups.

sufficient to produce measurable secondary oscillations. The activation threshold for the PMMA-Hexadecane capsules, clearly visible in figure 4(f), is 150 mJ cm^{-2}.

The average peak-to-peak acoustic emission from the microcapsules in response to laser activation (PA response) for each energy setting is plotted in figure 5 together with that of a gold nanospheres suspension whose absorbance has been matched to the capsules sample.

Figure 5 illustrates the photoacoustic strength of these vaporization agents above their activation threshold as compared to gold nanoparticles. More importantly, figure 5 demonstrates the positive effect of both, a reduction of the boiling point of the liquid and of a Janus configuration on the photoacoustic strength of the particles. The peak pressures ratio displayed in figure 4(e) suggests that gold nanoparticles start inducing cavitation above ∼120 mJ cm^{-2}, and on the contrary to the polymeric particles, the photoacoustic response of the gold nanoparticles remains quasi-linear as a function of the laser energy beyond cavitation inception.

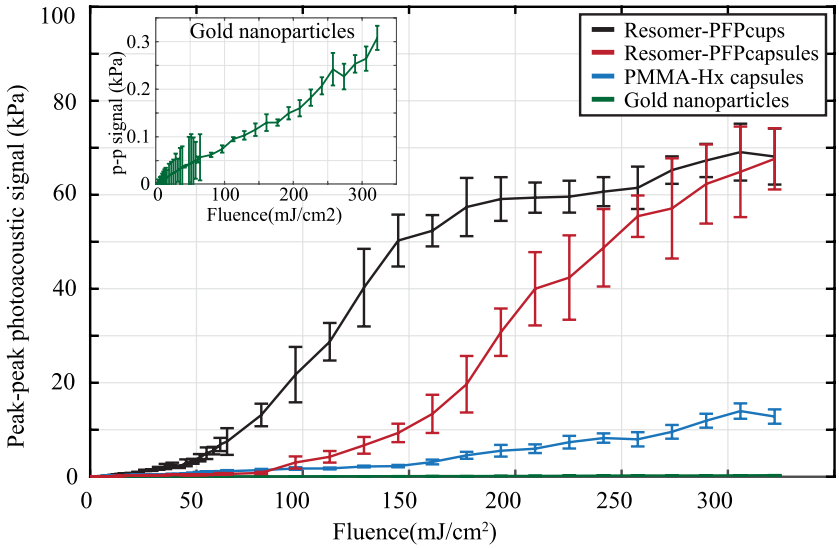

Figure 5. PA response for increasing laser fluence. PA responses for PMMA-hexadecane capsules containing 5% dye, of Resomer-PFP particles containing 5% dye (capsules and cups) and of gold nanoparticles. The solid lines represent the average over eight recordings and the error bars are the standard deviation over these eight experiments. The inset is a zoom of the photoacoustic response of the gold nanoparticles.

3.2. Microbubble generation from single microcapsules

Experiments with single microcapsules were performed to measure cavitation probability and stable bubble probability and size. The probability of activation of Resomer-PFP capsules, shown in figure 6(a), approaches 100% already at a fluence of 96 mJ cm^{-2}. The fraction of cavitating capsules that produce transiently stable bubbles gradually increases from ∼10% at 60 mJ cm^{-2} to ∼80% at 240 mJ cm^{-2}. A fluence of 1200 mJ cm^{-2} results in less bubbles surviving, which we attribute to the extreme violence of the cavitation events. Figure 6(b) displays the average bubble size after activation, which slowly increases from 1.8 μm at 60 mJ cm^{-2} to just under 3 μm, for fluences of 120 mJ cm^{-2} and higher.

The size of the bubbles produced by Resomer-PFP cups is similar to those generated by the capsules. From the sizes displayed in figure 6(b) and equation (3), the bubbles created by the cavitation events of PFP-loaded capsules and cups are expected to resonate around 1 MHz.

As seen in figure 4, PMMA-Hexadecane capsules require a much higher fluence before reaching their activation threshold. Activation, in the case of PMMA-Hexadecane capsules, rarely resulted in a stable bubble. In this case, a size of approximately 1.5–2 μm in radius hints at an acoustic activity predominantly around a frequency of 2 MHz.

3.3. Acoustic scattering

The bubbles were probed with a chirp, in the setup of figure 2(a), sweeping the frequencies from 0.3 to 2.3 MHz. Figure 7 displays the acoustic scatter maps and the simulated scatter map for the Resomer-PFP capsules.

The experimental and simulated scatter map displayed in figures 7(d) and (e) agree well. In both cases, the frequency of maximum response is about 1 MHz and the bandwidth is comparable: 0.6–2.2 MHz for the computed map and a 0.6–1.9 MHz for the measured map. The 1 MHz center frequency corresponds to a ∼3.3 μm radius bubble (estimated from equation (3)). The computed map displays, however, a slightly lower threshold than the experimental results.

The acoustic activity of the Resomer-PFP cups (see figure 7(c)) is very similar to that of the capsules in terms of center frequency, bandwidth, and onset of acoustic activity. The maximum received pressure by the transducer in both cases is ∼2 kPa, corresponding to 2% of the transmit pulse. The root mean square error between the measured maps and the calculated map scaled to the magnitude of the measured maps is, in both cases about 17%.

Laser activation of PMMA-hexadecane microcapsules lead to a very different result. First, the pressure received is an order of magnitude lower, 0.35 kPa, see figure 7(b). Secondly, the center frequency of the response lies around 1.7 MHz, indicating significantly smaller bubbles (∼1.8 μm radius), which is also consistent with figure 6(b). The scatter signal of PMMA-hexadecane capsules increases from 150 mJ cm^{-2} onwards, which corresponds to the cavitation threshold observed in photoacoustic emission.

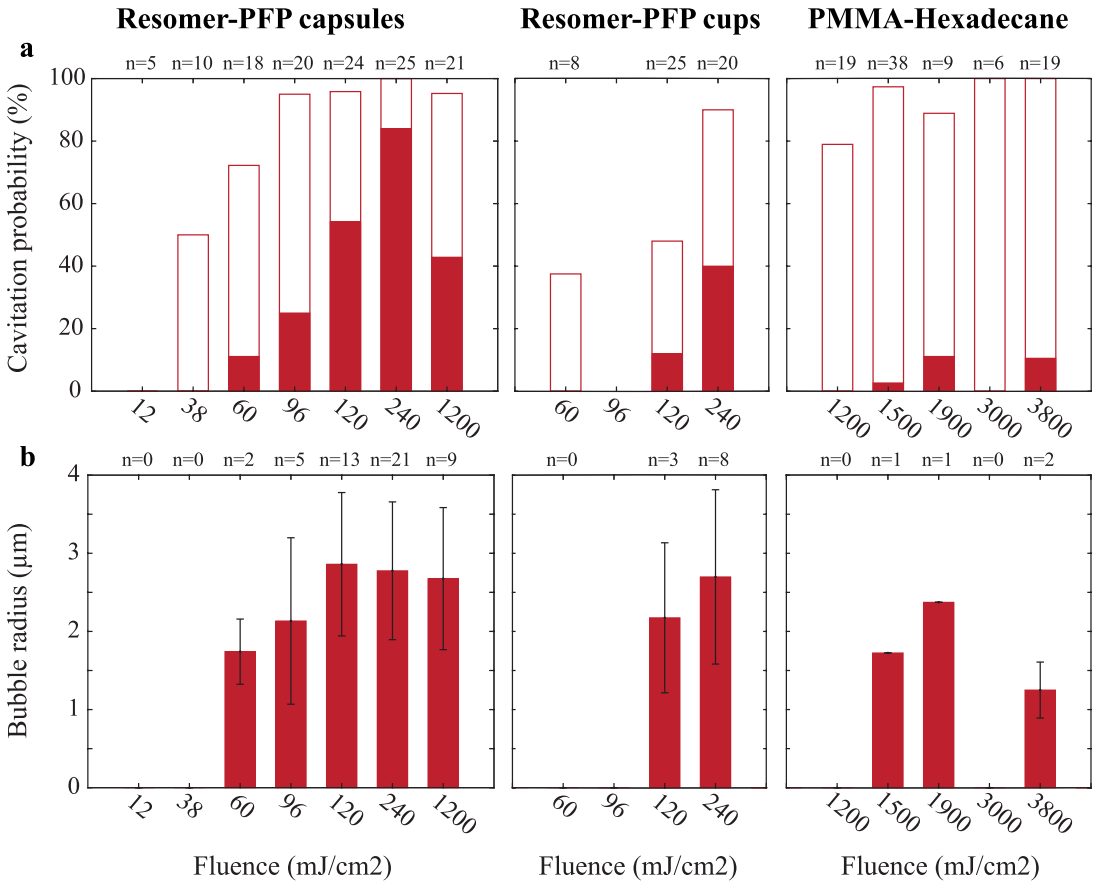

Figure 6. Probability and size of the created bubbles. (a) Cavitation probability of the capsules (filled red bar), and probability of the activation resulting in a stable bubble, (empty red bars), (b) mean radius of remaining bubbles and the standard deviation of this radius (error bars) calculated on the number of experiments indicated above each bar.

The reference measurements, performed in pure water and with AuNP (figure 7(a)), produced no measurable US scatter, despite the evidence of cavitation from the gold nanoparticles visible in figure 4(e), suggesting that the bubbles created by the nanoparticles are purely transient.

3.4. Temperature effect

To mimic more clinically relevant temperature conditions, the experiments were performed at a temperature of 37 °C. The result of the PA response is displayed in figures 8(a) and (d). The response of the PMMA-hexadecane capsules is slightly increased at higher temperature. Increasing the medium temperature lowers the difference between the capsule vaporization temperature threshold and the ambient temperature. The activation energy is thereby reduced and the laser energy threshold decreases accordingly (from 150 mJ cm^{-2} to 133 mJ cm^{-2}). Thus, the observation is in line with the theoretical prediction. At a given ambient temperature T_r, and assuming a constant light absorption coefficient α and heat capacity c_p:

$$E_{asb}(T_r) = \alpha E_{laser} = \rho V c_p (T_a - T_r). \tag{7}$$

The 2 measured energy thresholds therefore provide a rough estimate of the activation temperature:

$$T_a = \frac{E_2 T_{r1} - E_1 T_{r2}}{E_2 - E_1} \approx 154\ ^\circ\mathrm{C} \tag{8}$$

where $T_{r1} = 22\ ^\circ$C and $T_{r2} = 37\ ^\circ$C are the two experimental ambient temperatures and E_1 and E_2 are the two energy thresholds for cavitation, at those ambient temperatures.

First order thermodynamics considerations (detailed in SI-5) dictate that the Resomer-PFP capsules should display a plateau in their response, as a function of the laser energy, and that the plateau temperature for the polymer shell decreases linearly with the bath temperature.

Using the glass transition of the Resomer $T_{g,Res} = 50\ ^\circ$C and the activation energy of $E_a = 75$ mJ cm^{-2} at ambient temperature $T_{r1} = 22\ ^\circ$C in combination with a plateau temperature of $T_{plateau} = 117\ ^\circ$C for a bath temperature $T_{r2} = 37\ ^\circ$C (see SI-5) leads to a laser energy $E_{plateau}$:

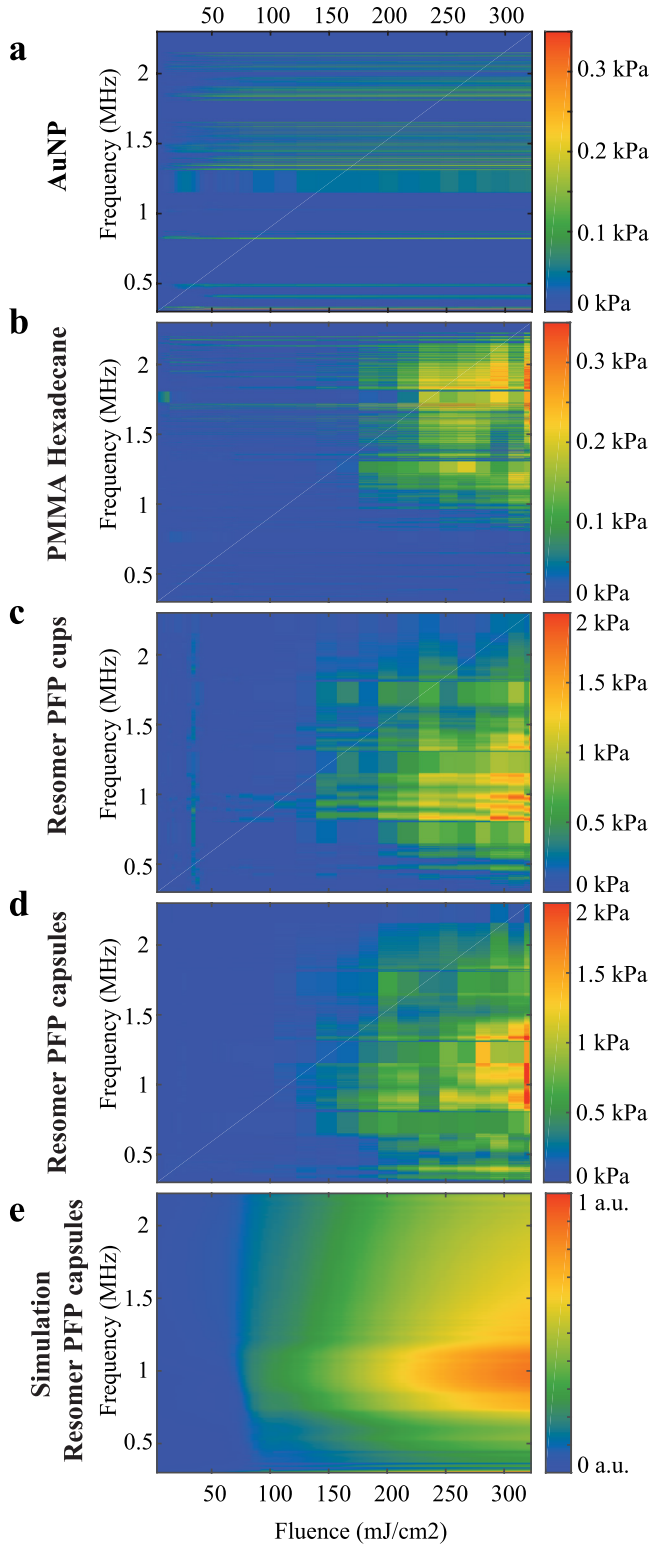

Figure 7. Scattered pressure map. Received pressure as a function of US frequency and laser fluence for (a) AuNP, (b) PMMA-hexadecane capsules, (c) Resomer-PFP cups, (d) Resomer-PFP capsules, and (e) theoretical prediction for Resomer-PFP capsules.

$$E_{plateau} = \frac{T_{plateau} - T_{r2}}{T_{g,Res} - T_{r1}} E_a = 214 \text{ mJ cm}^{-2}, \quad (9)$$

which agrees well with figure 8(d).

The scattering at body temperature is shown in figures 8(b), (c), (e) and (f). The center frequency scattered by the bubble created from the PMMA-hexadecane capsules shifts from 1.7 to 1.4 MHz at 37 °C, see figure 8(c). This result suggests that the temperature increase causes an increase of the transiently stable bubble size by ~20%. For the Resomer-PFP capsules the frequency shift with temperature is not significant, see figure 8(f).

The amplitude of the scattered pressure for Resomer-PFP capsules, follows the same trend as the PA response, compare figures 8(d) and (e). PMMA-hexadecane capsules display no significant change in scattered pressure amplitude with temperature, even though the PA response was higher at 37 °C. This lack of temperature dependence indicates that the number of residual bubbles is similar at both temperatures.

4. Discussion

In this study, we investigated the feasibility of multimodal imaging with two formulations of microcapsules, PMMA-hexadecane and Resomer-PFP, and we found that both enhance contrast in PA and US as compared to AuNPs.

The single-capsule experiments performed on PMMA-hexadecane capsules showed limited response and almost no remaining stable bubbles. Nonetheless, the PA pulse showed a tri-polar response indicating transient bubble formation. This emission is probably produced by a small amount of capsules with more dye and thus a higher absorption than the average capsule.

Also the PA signal showed transition to a tripolar pulse above ∼150 mJ cm^{-2}. These oscillations and the corresponding remaining bubbles are attributed to the exchange of dissolved gas in the liquid by the vapor bubble during the initial cavitation event. Gas exchange leads to the creation of a stable gas bubble (Suslick *et al* 1990, Leighton 1995) that requires time to dissolve back into the medium (Epstein and Plesset 1950). In the present case, dissolution of the gas bubble is further slowed down by the local heating of the surrounding liquid, which reduces the saturation concentration of dissolved gases (Suslick *et al* 1990, Leighton 1995). The details of this process require further investigation.

The lower amplitude of the third peak in the PA response of the Resomer-PFP capsules, in combination with the strong secondary oscillations, clearly indicates that the collapse of the cavitation bubble is dampened by a transiently stable gas bubble. Furthermore, the lower frequency of these oscillations, as compared to the ringing generated by PMMA-hexadecane, hints to the formation of larger bubbles (Szabo 2004), which is consistent with the vaporization of a volatile oil core.

The amplitude response of the Resomer-PFP cups is higher than that of the capsules. This can be partially caused by their lower activation threshold. Even though the PA response was higher and showed a lower threshold for the cups than for the capsules, the pulse-echo signal strength is similar (see figures 5 and 7(c), (d)). Thus, the probability of producing a stable remaining bubble is likely to be marginally lower for the cups than for the capsules.

According to the current hypothesis (Lajoinie *et al* 2014), nucleation of the capsules is triggered when the polymer shell melts. Therefore, in an ideal case, these light-absorbing microcapsules should display a step response as a function of the laser energy rather than a gradual increase as is observed here. We attribute this smoothing out of the response to a variability of the capsules absorption yield and its size within the probed volume.

The data from the single capsule experiments were used to compute the simulated pressure response map for Resomer-PFP capsules. This was not done for the other particles because of the limited statistical relevance of the data collected. The geometry of the Resomer-PFP cups also complicates the observation as the oil droplet core often faces downwards by gravity, and is therefore partially occluded by the polymer. The orientation of the cups may have resulted in unaccounted cavitation events.

Microbubbles used as US contrast agents, rely on their second harmonic or subharmonic backscatter to improve contrast (Shekhar *et al* 2014). In our experiments, chirps were used to probe the bubble oscillations. During the eight chirps sent, no significant harmonics were observed in the backscattered signals (Borsboom *et al* 2005).

In the current study we have used mono-disperse particles, resulting in a mono-disperse stable bubbles and thus consistent US scattering. However, the US scattering properties of the capsules is expected to change by altering the size of the capsules. The US scattering properties are directly related to the size of the bubbles produced upon photoacoustic activation. The bubble size is correlated to the volume available for vaporization, either encapsulated in the case of the low boiling point core capsules, or by the surface area of the particles in case of a high boiling point core.

Previous studies have investigated bubble–bubble interactions within a bubble cloud (Testud-Giovanneschi *et al* 1990, Kurz and Thomas 2010, Tinne *et al* 2010, Yoichiro and Shin 0000). Most of these studies are based on the bubble–bubble interaction between two bubbles and report asymmetry, deformation and attraction (Testud-Giovanneschi *et al* 1990). These interactions between bubbles can be experienced up to a distance of 10 radii (Testud-Giovanneschi *et al* 1990, Tinne *et al* 2010). Despite the statistically large inter-bubble distance, >30× their radius (see SI-4 for justification), we cannot rule out a hypothetical influence of these interactions, owing to the statistical nature of this argument, and to the large size of the initial cavitation bubbles. Coalescence can also not be ruled out at this stage, although no direct evidence of it has been observed.

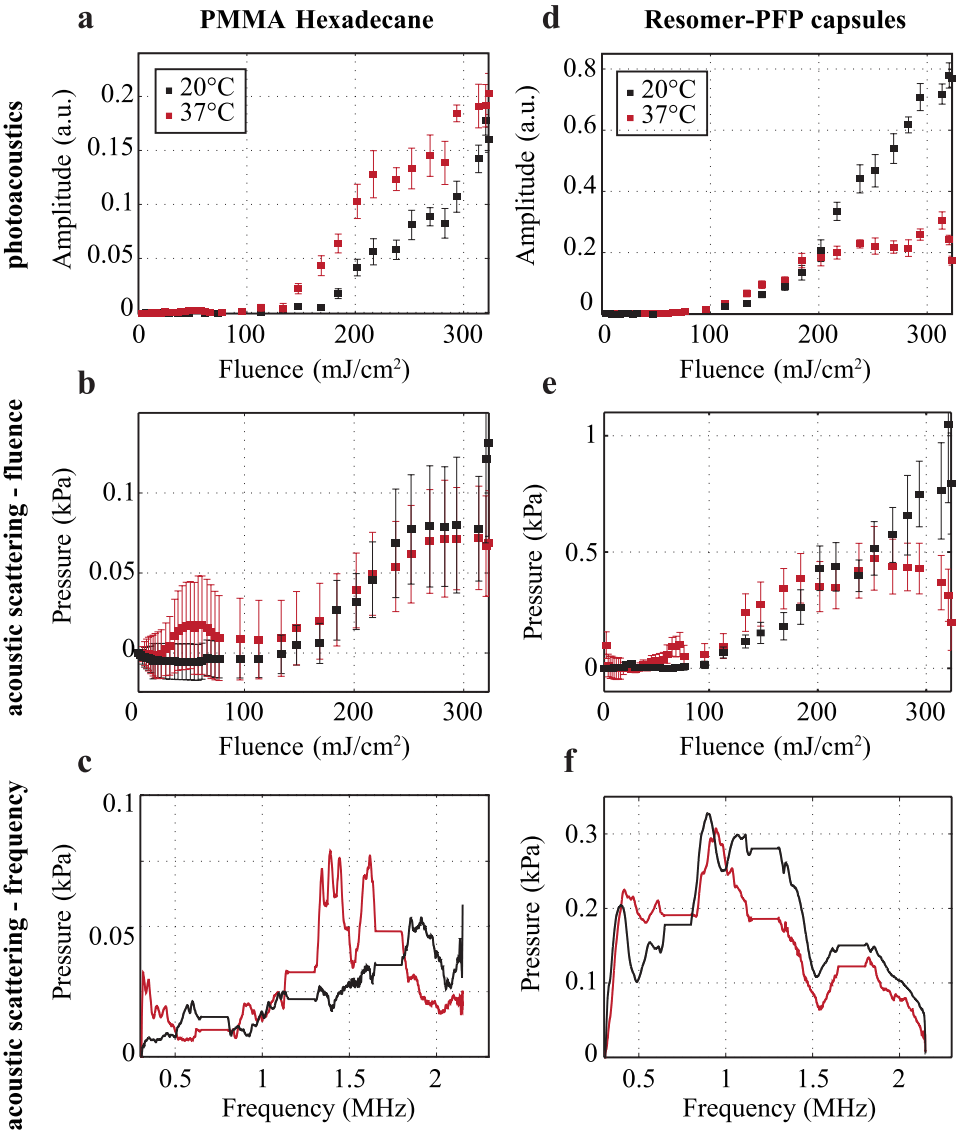

Figure 8. Response of laser activated capsules at 20 °C and 37 °C Resomer-PFP capsules. (a) PA response. (b) Pulse-echo response, average received pressure, for increasing fluence. (c) Pulse-echo response, average received pressure, for different frequencies. PMMA-hexadecane capsules. (d) PA response. (e) Pulse-echo response, average received pressure, for increasing fluence. (f) Pulse-echo response, average received pressure, for different frequencies.

First order thermodynamics considerations detailed in SI-5 justify the existence of a plateau in figure 8(d) and predict its position. The signal amplitude, however, is expected to reach similar values in both cases but appear to be significantly lower at 37 °C than at 20 °C. This may be a sign of spontaneous activation of a fraction of the agents during the incubation at 37 °C, leaving less capsules available for laser activation.

The absence of temperature effect on the frequency of the maximum US scatter is consistent with the vaporization of a preexisting, volume-limited volatile core. Vaporizing water (as is the case for the PMMA-hexadecane capsules) requires much more energy than vaporizing PFP. Therefore, at energies around the activation threshold of the PFP-filled particles, only the volatile core is vaporized, which result in bubbles with a constant size (neglecting thermal dilation). Subsequently, the US frequency response remains unchanged.

Currently, these first formulations of PFP-loaded particles still present activations thresholds that are slightly elevated in view of medical safety recommendations. However, the improved response over traditional agents make them promising for clinical applications, since the probability of a vaporization event and the probability of producing a stable bubble are high. The threshold for the activation of these capsules can be further reduced by increasing the dye loading efficiency of the polymer shell. Other possibilities to reduce the threshold would be a liquid core with a lower boiling point and a polymer with a lower glass transition temperature.

Additionally, the dye could be replaced by a dye absorbing in the NIR or IR range, thereby increasing the MPE. This would be beneficial in terms of imaging depth as well.

5. Conclusions

The results of our study demonstrate that both PMMA-Hexadecane and Resomer-PFP particles in suspension are capable of enhancing multimodal contrast in a combined US and PA imaging modality. However, the threshold and signal strength of PFP-loaded capsules were shown to be more advantageous. For PFP-loaded capsules, the PA activation threshold was found to be around the medically relevant values and the US scatter was readily measured and proved to be maximum at medically relevant frequencies. The surrounding temperature was shown to affect both the maximum PA signal and US contrast generation from Resomer-PFP capsules and the proposed agents display an increased efficiency at body temperature. The response of the capsules to a laser pulse can be advantageously combined with US to increase the amount of information provided by the contrast agents.

Acknowledgment

This work is supported by NanoNextNL, a micro and nanotechnology consortium of the Government of the Netherlands and 130 partners. The authors gratefully acknowledge the technical support of Bas Benschop, Martin Bos and Gert-Wim Bruggert.

ORCID iDs

Mirjam Visscher https://orcid.org/0000-0002-6867-7398
Guillaume Lajoinie https://orcid.org/0000-0002-8226-7301
Michel Versluis https://orcid.org/0000-0002-2296-1860

References

Bayer C L, Chen Y-S, Kim S, Mallidi S, Sokolov K and Emelianov S 2011 Multiplex photoacoustic molecular imaging using targeted silica-coated gold nanorods *Biomed. Opt. Exp.* **2** 1828–35
Bell A G 1880 Upon the production and reproduction of sound by light *J. Soc. Telegraph Eng.* **9** 404–26
Bhattacharyya S, Wang S, Reinecke D, Kiser W Jr, Kruger R A and DeGrado T R 2008 Synthesis and evaluation of near-infrared (nir) dye-herceptin conjugates as photoacoustic computed tomography (pct) probes for her2 expression in breast cancer *Bioconjugate Chem.* **19** 1186–93
Borsboom J M G, Chin C T, Bouakaz A, Versluis M and de Jong N 2005 Harmonic chirp imaging method for ultrasound contrast agent *IEEE Trans. Ultrason. Ferroelectr. Freq. Control* **52** 241–8
Calliada F, Campani R, Bottinelli O, Bozzini A and Sommaruga M G 1998 Ultrasound contrast agents: basic principles *Eur. J. Radiol.* **27** S157–60
Chen H, Kreider W, Brayman A A, Bailey M R and Matula T J 2011 Blood vessel deformations on microsecond time scales by ultrasonic cavitation *Phys. Rev. Lett.* **106** 34301
Chen X, Schwarz K Q and Parker K J 1994 Acoustic coupling from a focused transducer to a flat plate and back to the transducer *J. Acoust. Soc. Am.* **95** 3049–54
Choi J J, Selert K, Vlachos F, Wong A and Konofagou E E 2011 Noninvasive and localized neuronal delivery using short ultrasonic pulses and microbubbles *Proc. Natl Acad. Sci.* **108** 16539–44
De Jong N 1993 Acoustic properties of ultrasound contrast agents *PhD Thesis* Erasmus MC: University Medical Center Rotterdam
Deckers R, Rome C and Moonen C T W 2008 The role of ultrasound and magnetic resonance in local drug delivery *J. Magn. Reson. Imaging* **27** 400–9
Doinikov A A, Haac J F and Dayton P A 2009 Resonance frequencies of lipid-shelled microbubbles in the regime of nonlinear oscillations *Ultrasonics* **49** 263–8
Epstein P S and Plesset M S 1950 On the stability of gas bubbles in liquid–gas solutions *J. Chem. Phys.* **18** 1505–9
Frenkel V 2008 Ultrasound mediated delivery of drugs and genes to solid tumors *Adv. Drug Deliv. Rev.* **60** 1193–208
Hilgenfeldt S, Brenner M P, Grossmann S and Lohse D 1998 Analysis of Rayleigh–Plesset dynamics for sonoluminescing bubbles *J. Fluid Mech.* **365** 171–204
Husseini G A and Pitt W G 2009 Ultrasonic-activated micellar drug delivery for cancer treatment *J. Pharm. Sci.* **98** 795–811
Hynynen K, McDannold N, Vykhodtseva N, Raymond S, Weissleder R, Jolesz F A and Sheikov N 2006 Focal disruption of the blood–brain barrier due to 260 kHz ultrasound bursts: a method for molecular imaging and targeted drug delivery *J. Neurosurg.* **105** 445–54
Jeon M *et al* 2014 Methylene blue microbubbles as a model dual-modality contrast agent for ultrasound and activatable photoacoustic imaging *J. Biomed. Opt.* **19** 016005
Keller J B and Miksis M 1980 Bubble oscillations of large amplitude *J. Acoust. Soc. Am.* **68** 628–33
Khanna P, Ong C, Bay B H and Baeg G H 2015 Nanotoxicity: an interplay of oxidative stress, inflammation and cell death *Nanomaterials* **5** 1163–80
Kim G, Huang S-W, Day K C, O'Donnell M, Agayan R R, Day M A, Kopelman R and Ashkenazi S 2007 Indocyanine-green-embedded pebbles as a contrast agent for photoacoustic imaging *J. Biomed. Opt.* **12** 044020
Lauterborn W and Kurz T 2010 Physics of bubble oscillations *Rep. Prog. Phys.* **73** 106501
Lajoinie G, Gelderblom E, Chlon C, Böhmer M, Steenbergen W, de Jong N, Manohar S and Versluis M 2014 Ultrafast vapourization dynamics of laser-activated polymeric microcapsules *Nat. Commun.* **5** 3671
Lajoinie G, Lee J Y, Owen J, Kruizinga P, de Jong N, van Soest G, Stride E and Versluis M 2017a Laser-driven resonance of dye-doped oil-coated microbubbles: experimental study *J. Acoust. Soc. Am.* **141** 4832–46

Lajoinie G, Linnartz E, Kruizinga P, de Jong N, Stride E, van Soest G and Versluis M 2017b Laser-driven resonance of dye-doped oil-coated microbubbles: a theoretical and numerical study *J. Acoust. Soc. Am.* **141** 2727–45
Leighton T 1995 Bubble population phenomena in acoustic cavitation *Ultrason. Sonochem.* **2** S123–36
Leighton T G 1994 Acoustic bubble detection-I. The detection of stable gas bodies *Environmental engineering* **7** 9–16
Li P-C, Wei C-W, Liao C-K, Chen C-D, Pao K-C, Wang C-R C, Wu Y-N and Shieh D-B 2006 Multiple targeting in photoacoustic imaging using bioconjugated gold nanorods *Photons Plus Ultrasound: Imaging and Sensing 2006: the 7th Conf. on Biomedical Thermoacoustics, Optoacoustics, and Acousto-optics* vol 6086 (International Society for Optics and Photonics) p 60860M
Loxley A and Vincent B 1998 Preparation of poly(methylmethacrylate) microcapsules with liquid cores *J. Colloid Interface Sci.* **208** 49–62
Lu W *et al* 2010 Photoacoustic imaging of living mouse brain vasculature using hollow gold nanospheres *Biomaterials* **31** 2617–26
Luke G P, Yeager D and Emelianov S Y 2012 Biomedical applications of photoacoustic imaging with exogenous contrast agents *Ann. Biomed. Eng.* **40** 422–37
Mallidi S, Kim S, Karpiouk A, Joshi P P, Sokolov K and Emelianov S 2015a Visualization of molecular composition and functionality of cancer cells using nanoparticle-augmented ultrasound-guided photoacoustics *Photoacoustics* vol 3 (special issue: contrast agents for optoacoustic imaging and sensing: design and biomedical applications) pp 26–34
Mallidi S, Larson T, Tam J, Joshi P P, Karpiouk A, Sokolov K and Emelianov S 2009 Multiwavelength photoacoustic imaging and plasmon resonance coupling of gold nanoparticles for selective detection of cancer *Nano Lett.* **9** 2825–31
Mallidi S, Luke G P and Emelianov S 2011 Photoacoustic imaging in cancer detection, diagnosis, and treatment guidance *Trends Biotechnol.* **29** 213–21
Mallidi S, Watanabe K, Timerman D, Schoenfeld D and Hasan T 2015b Prediction of tumor recurrence and therapy monitoring using ultrasound-guided photoacoustic imaging *Theranostics* **5** 289
Michaels J E, Lee S J, Croxford A J and Wilcox P D 2013 Chirp excitation of ultrasonic guided waves *Ultrasonics* **53** 265–70
Overvelde M, Garbin V, Sijl J, Dollet B, de Jong N, Lohse D and Versluis M 2010 Nonlinear shell behavior of phospholipid-coated microbubbles *Ultrasound Med. Biol.* **36** 2080–92
Prosperetti A and Lezzi A 1986 Bubble dynamics in a compressible liquid *J. Fluid Mech.* **168** 457–78
Shekhar H, Awuor I, Thomas K, Rychak J J and Doyley M M 2014 The delayed onset of subharmonic and ultraharmonic emissions from a phospholipid-shelled microbubble contrast agent *Ultrasound Med. Biol.* **40** 727–38
Shih R, Bardin D, Martz T D, Sheeran P S, Dayton P A and Lee A P 2013 Flow-focusing regimes for accelerated production of monodisperse drug-loadable microbubbles toward clinical-scale applications *Lab Chip* **13** 4816–26
Sijl J, Gaud E, Frinking P J A, Arditi M, de Jong N, Lohse D and Versluis M 2008 Acoustic characterization of single ultrasound contrast agent microbubbles *J. Acoust. Soc. Am.* **124** 4091–7
Stantz K M, Cao M, Liu B, Miller K D and Guo L 2010 Molecular imaging of neutropilin-1 receptor using photoacoustic spectroscopy in breast tumors *Photons Plus Ultrasound: Imaging and Sensing* vol 7564 (International Society for Optics and Photonics) p 75641O
Suslick K, Doktycz S and Flint E 1990 On the origin of sonoluminescence and sonochemistry *Ultrasonics* **28** 280–90
Szabo T L 2004 *Diagnostic Ultrasound Imaging: Inside Out* (New York: Academic)
Testud-Giovanneschi P, Alloncle A P and Dufresne D 1990 Collective effects of cavitation: experimental study of bubble–bubble and bubble-shock wave interactions *J. Appl. Phys.* **67** 3560–4
Tinne N, Schumacher S, Nuzzo V, Arnold C L, Lubatschowski H and Ripken T 2010 Interaction dynamics of spatially separated cavitation bubbles in water *J. Biomed. Opt.* **15** 68003–10
Versluis M, Schmitz B, von der Heydt A and Lohse D 2000 How snapping shrimp snap: through cavitating bubbles *Science* **289** 2114–7
Wei K-C *et al* 2013 Focused ultrasound-induced blood–brain barrier opening to enhance temozolomide delivery for glioblastoma treatment: a preclinical study *PLoS One* **8** e58995
Wilson K, Homan K and Emelianov S 2010 Photoacoustic and ultrasound imaging contrast enhancement using a dual contrast agent *Photons Plus Ultrasound: Imaging and Sensing* vol 7564 (International Society for Optics and Photonics) p 75642P
Wilson K, Homan K and Emelianov S 2012 Biomedical photoacoustics beyond thermal expansion using triggered nanodroplet vaporization for contrast-enhanced imaging *Nat. Commun.* **3** 618
Wu M, Springeling G, Lovrak M, Mastik F, Iskander-Rizk S, Wang T, van Beusekom H M, van der Steen A and Van Soest G 2017 Real-time volumetric lipid imaging *in vivo* by intravascular photoacoustics at 20 frames per second *Biomed. Opt. Express* **8** 943–53
Yoichiro M and Shin Y 0000 Behaviour of a bubble cluster in an ultrasound field *Int. J. Numer. Methods Fluids* **47** 591–601
Yue X, Zhang Q and Dai Z 2017 Near-infrared light-activatable polymeric nanoformulations for combined therapy and imaging of cancer *Adv. Drug Deliv. Rev.* **115** 155–70 (Nanoformulations for combination or cascade anticancer therapy)